



## F4 hypersonic wind tunnel: coupled CFD-MHD-material simulation of the arc chamber focusing on the degradation of the electrodes

X. Lamboley. L. Serre. B. Khiar. N. Dellinger. J.-M. Lamet. J.-L. Vérant<sup>6</sup>

#### Abstract

The ONERA F4 hypersonic wind tunnel was commissioned in the early 1990s to support the European Space Shuttle program HERMES. Despite the cancellation of this program shortly afterwards, it has been used for many years to support studies of hypersonic reentry, both for Earth and Mars. More recently, it was used for scramjet propulsion tests in non water-viciated air. In this high-enthalpy wind tunnel, the hot flow source is generated using an electric arc chamber. This high-power arc (of the 150 MW class) heats a volume of a few litres of cold air at moderate pressure (between 30 and 80 bar) and brings it to the pressure and temperature levels required to simulate reentry conditions, with the ability to produce flows at several km/s. After a period of dormancy due to a slowdown in demand for tests in this speed range, the increasing focus on hypersonic high-enthalpy activities in France and worldwide in recent years justifies the reinstatement of this facility. This restart, which requires a partial renovation of the wind tunnel, also provides an opportunity to implement complementary activities aimed at better mastering the quality of the flow produced by the arc chamber. Indeed, the highpower electric arc heating process involves numerous physical phenomena, including the physics of the arc plasma, the Laplace forces that impact its dynamics, the interactions between the arc and the air, the dynamics of the internal air flow in the chamber, heat exchanges with the chamber walls and the degradation processes of the electrodes. The communication will first remind the design principles of the electrical architecture of the arc chamber, quided by the desire to minimise air pollution caused by electrode degradation. These architectural choices have been supported by large-scale experiments, which validated the principle of rotating the electric arc on its electrodes to limit degradation. In the second part, the article will present the work recently initiated at ONERA to start calculating the heating process in the arc chamber by coupling three in-house softwares: CEDRE for aero-thermochemistry and radiation, TARANIS for electromagnetism and MoDeTheC for material degradation processes. The first results obtained coupling these three codes will be presented. The final goal is to provide a better estimation of the flow properties when the pyrotechnic plug is activated to start the flow in the nozzle.

Keywords: Hypersonics, wind tunnel, F4, electric arc, CFD, MHD, material, code coupling, simulation

#### **Nomenclature**

```
Latin
                                                                        \overrightarrow{p} – momentum \lceil kq m s^{-1} \rceil
                                                                       T – temperature [K]
\overrightarrow{B} – magnetic field [T]
                                                                       U – voltage [V]
E – energy [J]
                                                                       V – volume [m<sup>3</sup>]
I - current [A]
                                                                       \overrightarrow{V} – velocity [m s^{-1}]
p - pressure [Pa]
                                                                       \overrightarrow{x} – position of nodes [m]
P - power [Js^{-1}]
```

HiSST-2025-79 Copyright © 2025 by the author(s)

<sup>&</sup>lt;sup>1</sup>ONERA Department Multi-Physics for Energetics, xavier.lamboley@onera.fr

<sup>&</sup>lt;sup>2</sup>ONERA Defense Programes Directorate, laurent.serre@onera.fr

<sup>3</sup> ONERA Department Physics, Instrumentation, Environment and Space, benjamin.khiar@onera.fr

<sup>&</sup>lt;sup>4</sup>ONERA Department Multi-Physics for Energetics, nicolas.dellinger@onera.fr

<sup>&</sup>lt;sup>5</sup>ONERA Department Multi-Physics for Energetics, jean-michel.lamet@onera.fr

<sup>&</sup>lt;sup>6</sup>ONERA Department Multi-Physics for Energetics, jean-luc.verant@onera.fr

```
\begin{array}{lll} Y_s - \text{ species mass fraction} & Subscripts \\ & Greek & \text{m - mass} \\ \epsilon - \text{ emissivity} & \text{e - energy} \\ \varepsilon - \text{ porosity} & \text{conv - convective} \\ \varphi - \text{ heat flux } [\text{W m}^{-2}] & \text{rad - radiative} \\ \sigma - \text{ electrical conductivity } [\text{S m}^{-1}] & \text{cond - conductive} \end{array}
```

## 1. History of the F4 arc chamber

#### 1.1. Initial reflections on arc chamber architecture

At the onset of designing the arc chamber's architecture, ONERA began by surveying various options previously employed in somewhat similar testing facilities, notably those of NASA. These were mostly powered by capacitor banks, delivering extremely high currents over very short durations. The current source ONERA intended to utilise was an existing impulsive machine, where energy was stored in a flywheel coupled with a winding and thyristor system, enabling the flywheel to reach speeds of up to approximately  $6000\,\mathrm{rpm}$  before recovering the energy as direct current. The electrical and mechanical characteristics of this setup leaned more towards powers in the class of  $160\,\mathrm{MW}$ , relatively stable operating conditions in voltage and current ( $4\,\mathrm{kV}$  /  $40\,\mathrm{kA}$ ) and longer operating durations compared to the more impulsive American installations.

Thus, studies aimed to capitalise on these constraints to achieve a heating as homogeneous as possible while avoiding contamination by particles from the walls or electrodes. The selection of materials for the electrodes led to a series of tests involving material samples under a  $10\,\mathrm{kW}$  CO<sub>2</sub> laser flux, designed to produce a thermal flux comparable to that expected in the arc chamber.

The candidate that emerged from these studies was a CuW composite, following analysis of various nuances concerning the fractions of Cu and W. However, the primary structuring activity for the arc chamber was to choose an electrical architecture capable of ensuring stable and homogeneous heating of a roughly ten-liter chamber, while minimising electrode degradation.

Several key questions had to be addressed, which became high-level specifications. These included:

- ensuring the arc occupies most of the chamber volume to limit the risk of creating "cold spots";
- preventing the arc foot from attaching to the electrodes to limit the risk of fusion;
- correctly mastering the power delivery law to the fluid to limit dispersions in conditions obtained at arc extinction;
- allowing for reliable ignition of the arc regardless of initial fill pressure levels (in air, nitrogen, CO<sub>2</sub>, etc);
- facilitating necessary checks on electrodes, joints, etc. thus enabling multiple tests per day if required;
- minimising electromagnetic disturbances that the arc chamber's operation could induce on nearby equipment, particularly instrumentation.

To satisfy these constraints, it seemed interesting to seek an electrical configuration that is globally as close as possible to a coaxial architecture.

## 1.2. Coaxial architecture principle

The scheme on figure 1a illustrates this principle. Two electrodes face each other at each end of the chamber. They are supplied along their axis, but only the ring-shaped part constitutes the electrode; the rest of the circuit is under thermal and electrical insulation (thermally and electrically protected). The current arrives on the chamber's axis and joins the center of the first electrode. It is then conducted to the external circular ridge, which is actually a conductive spiral that remains open at its end. The arc crosses the arc chamber to reach the external track of the opposite electrode, perfectly symmetrical to the first. Upon exiting this device, the current is distributed across six star-disposed bars allowing

it to return near the first electrode and close the circuit towards the initial supply bar using a second six-branch collector.

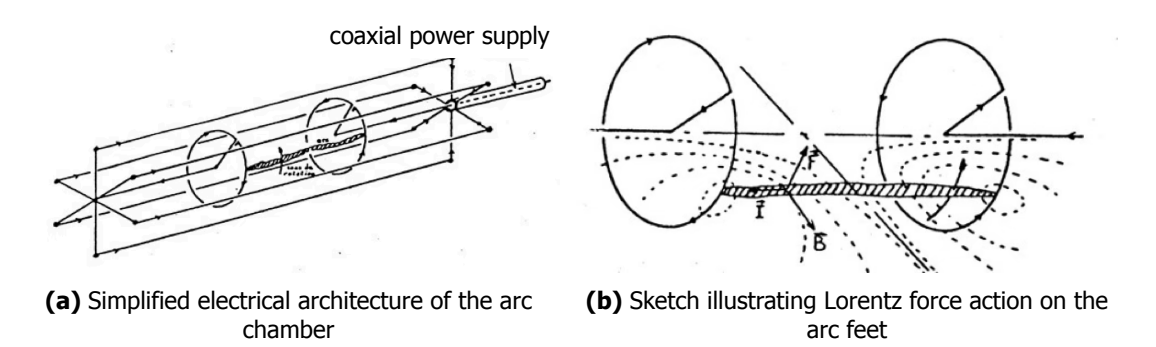


Fig 1. Diagrams of the operating principle of the arc chamber of the F4 facility (ONERA archives 1990)

#### 1.3. Simplified electrical architecture of the arc chamber

The expected benefits of this configuration are as follows:

- centralised arc tendency: a repulsive reaction in one of the return branches tends to keep the arc centred within the chamber if it approaches either branch;
- comprehensive chamber volume scanning by arc plasma: the large diameter of the electrodes ensures that the arc plasma sweeps across the entire volume of the chamber;
- rapid arc foot movement on electrodes: Lorentz forces induced on the arc by the pseudocoil formed by the internal electrical circuit of each electrode (see figure 1b) result in swift movement of the arc foot along the electrodes.

The symmetry between the two electrodes ensures that Lorentz forces push both arc feet in the same direction, thereby facilitating its rotation.

Before confirming the choice of this architecture for the operational chamber and defining technological solutions suitable for implementation in an enclosure operating up to  $2000\,\mathrm{bar}$ , it seemed necessary to verify beforehand that the underlying principles could indeed offer the expected benefits. To this end, a 1:1 scale experiment was conducted under electrical conditions representative of the targeted operational conditions but at atmospheric pressure. This approach allowed for freedom from mechanical constraints and high-pressure concerns, direct observation of the arc and finer measurement of electrical parameters.

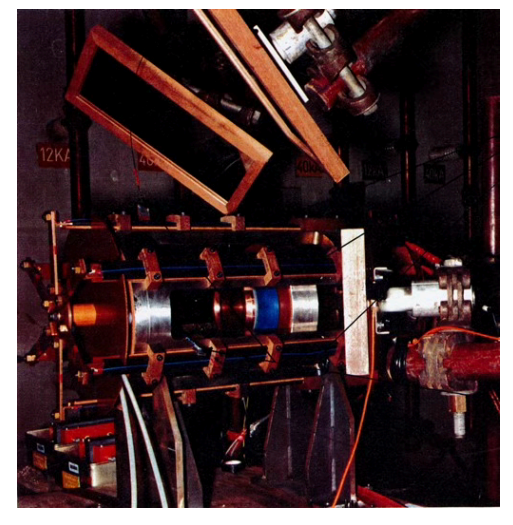
The test campaign was performed at EDF's (French National Electricity Company) Les Renardières center in 1990. The EDF research center was equipped with testing capabilities typically used for lightning studies or qualifying high-power components. Contrary to the planned DC setup for F4, tests were performed using  $50\,\mathrm{Hz}$  alternating current. The test rig was based on a modular design for the electrodes configuration, with either an electrode with internal winding and external cut spiral or a solid electrode. The chamber also had several variants:

- base structure with six ribs supporting the six return current bars;
- open cylindrical chamber usable as a return electrode with a central electrode;
- closed cylindrical chamber equipped with a calibrated leak to confine air and arc while limiting pressure increase;
- adjustable distance between electrodes (30 mm to 270 mm).

A custom instrumentation was developed for arc analysis. Voltage measurements could be performed either across each return current bar's terminals, or between the cut ends of the spirals constituting

the electrode. Observational tools include an optical fibre to observe transient arc breakout between support bars and if possible determine its rotational speed, and a set of mirrors reflecting towards a fast camera positioned on the chamber's axis for an overall view.





(a) Global view of the test rig

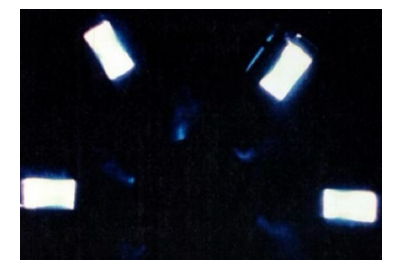
**(b)** Lateral view of the chamber in a two-electrode configuration

Fig 2. Views of the test rig at EDF Les Renardières test center in 1990

In the case of two electrodes facing each other inside an unconfined chamber, rapid camera observations were able to show good occupation of the chamber volume by the arc. The figure 3a shows the situation just after arc ignition on a fuse wire. The shape is initially very unstable, then stabilises with the rotation of the plasma in motion (figure 3b).



(a) At ignition



(b) Stabilized regime

Fig 3. Tests on long chamber (270 mm) at ignition and in stabilised regime

The figure 4a shows the two electrodes in the assembly version for tests in a pseudo-closed chamber, after a test. The pressure-limiting evacuation orifice is located in the upper left part of the wall. The thermal protection of the lower electrode has been removed and the internal metal spiral that reinforces the effect of the Lorentz forces already present with the external spiral (whose cut can also be seen at the end of the spiral) is clearly visible. The figure 4b shows the configuration with a single electrode and return of current in the wall, its path being left free. The image 4c shows the tendency of the arc to split into several branches and to rotate in the expected direction. However, this freedom given to the arc did not seem to favour the stability of the current or the homogeneity of heating for a closed chamber.



(a) Assembly for chamber with two electrodes



**(b)** Assembly with one electrode and return through the wall



(c) Stabilized regime

Fig 4. Assembly for configurations of the arc chamber with one or two electrodes

#### 1.4. Evidence of rotation in the coaxial cage bars

Measurements of potential differences at the terminals of different current bars between the entrance and exit of the area exposed to the arc reveal the evolution of current in these bars (figure 5). The overall pattern is, of course, that of a 50 Hz alternating current. Upon closer inspection of the signals, small oscillations of the current in the bars appear, which can provide an initial indication of an internal rotational movement of the arc carrying the total current. When comparing the signals corresponding to two diametrically opposed bars, it is observed that the oscillations are in opposite phase. This reinforces of a global oscillatory movement with opposite effects on current when closing or approaching a lateral current bar.

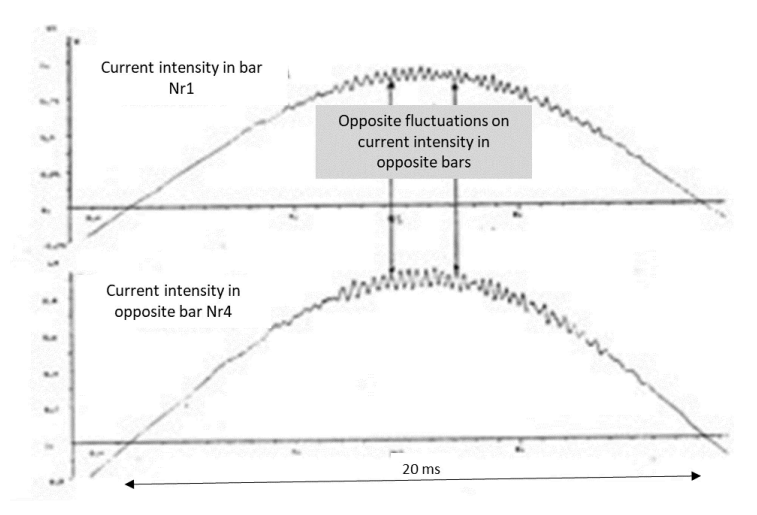


**Fig 5.** Illustration of the stabilising effects of the pseudo-coaxial cage architecture during a 20 ms half-period of alternative current test sequence (ONERA archives 1990)

The signal from the optical fibre also make it possible to highlight the rotation of the arc, with a completely different physical meaning. The comparison between a measurement based on the luminous flux and a measurement of voltage drop at the terminals of the cut at the end of the electrode's spiral showed an excellent correspondence between the oscillating phenomena. Naturally, the light signal is always positive, unlike the electrical measurements.

Based on this type of measurement, it was possible to plot the evolution of the observed arc rotation frequencies over several alternations during different tests performed for several current values on figure 6.

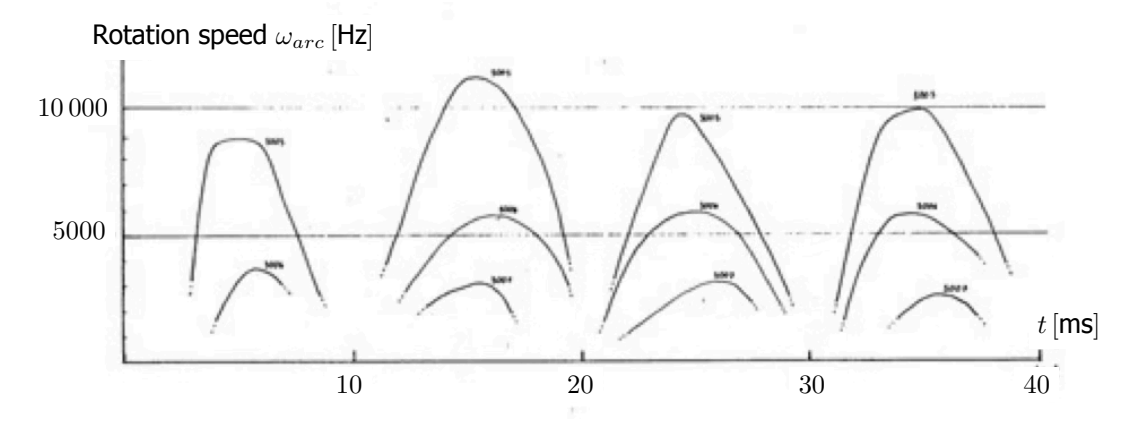


Fig 6. Measured rotation speed in different tests, with 3 levels of arc current (ONERA archives 1990)

We observe that the rotation frequency generally evolves with the intensity of the current, although the few tests performed do not really allow us to assert this. It would be tempting to conclude that we can assimilate the arc globally to a physical bar having an aerodynamic behaviour in which the speed is limited by drag, with a balance of Lorentz forces in  $I^2$  and aerodynamic forces in  $V^2$ . However, it was not possible to make such a direct link, knowing that the volumetric mass of very hot air in this highly turbulent environment was difficult to model. The future will tell if modern numerical means allow us to bring elements of appreciation on this hypothesis.

Another indicator of the effect of rotation on heating homogeneity is given by the configuration combining a spiral electrode (providing rotation of arc foot) and massive electrode for which the arc is free to attach over a large convex conducting surface. Figure 7 shows that the plasma covers a large part of the volume in the left part of the chamber, whereas it remains much more concentrated in the center part when let free.

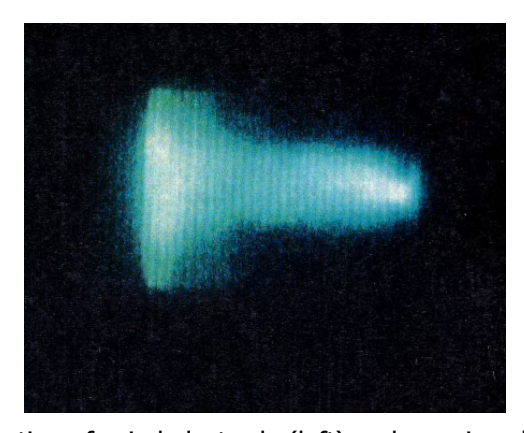


Fig 7. Combination of spiral electrode (left) and massive electrode (right)

## 1.5. Other observations

A few more observations have been made; firstly the arc re-ignites after extinction, indicating that the channel remains sufficiently conductive. This highlights the system's stability under test conditions. Moreover concerning the influence of the cut at the electrode end on the arc foot, no notable disturbance was observed, suggesting that the electrode design is effective in minimising undesirable interactions.

In the confined chamber configuration, key observations include that the walls, connected to ground with floating potential electrodes showed no signs of attachment. This validates the effectiveness of the configuration in avoiding parasitic interactions. Finally about the condition of the electrodes, they withstood the test campaign without damage or need for repair, demonstrating their robustness.

#### 1.6. Need for numerical simulation of the arc chamber

The tests at Les Renardières provided a solid experimental basis for validating the chosen options. The next step involves integrating these results into numerical simulations to explore the performance of the operational chamber, particularly with increasing pressure. This approach will combine experimental tests with advanced simulation tools to refine electrical parameters and predict arc behaviour under various operational conditions.

## 2. Coupled numerical simulation of the arc chamber

In parallel to the operational restart of the F4 high-enthalpy wind tunnel scheduled in 2026, modelling and numerical simulation activities have been initiated at ONERA in the scope of the HypHypF4 (Hypersonic Hyper-enthalpy F4) project, to better understand what happens inside the arc chamber during the heating phase. The aim is to characterise the state of the fluid at the end of the heating phase, in order to quantify pollution but also gas heating just before the expansion phase into the nozzle.

To achieve that, we firstly present here the code coupling strategy that was set up accounting for the different physics involved in the arc chamber; the computational approach involves the modelling of the air inside the arc chamber, the material around it for protection and the electrodes at the top and bottom of the chamber. Two approaches have been considered to model the energy provided by the electric arc, a first step using a volumetric source term of power in the CFD solver and a second step demonstrating a MHD/CFD coupled solution.

#### 2.1. Code coupling strategy

Inside the arc chamber occur a wide range of physics that are mandatory to take into account to be representative of high energy processes. A scheme summarising the solvers used upon the simulation and their couplings is presented in figure 8.

Fluid dynamics is represented by the CFD Finite-Volume solver *CHARME* [1, 2], part of the ONERA multiphysics *CEDRE* platform. Given the very high temperatures reached in the chamber the radiative transfer due to the molecules, atoms and ions have to be accounted for: this is done by the Monte-Carlo solver *ASTRE* [3, 4, 5] which is also part of the *CEDRE* platform.

The outer boundary of the chamber is made up of a carbon composite liner which will withstand high levels of convective and radiative fluxes that lead to its degradation. Heating and ablation processes of the liner are solved with ONERA *MoDeTheC* solver [6, 7, 8] using the Finite-Volume method. The final goal of such simulation is to quantify the pollution of the flow caused by the degradation of the electrodes. Electrodes heating and ablation is thus also modelled with *MoDeTheC*.

All of these solvers are of course interdependent, requiring a data exchange strategy between them. This is performed by the *cwipi* library developed at ONERA [9], which allows to exchange data between the surfacic or volumetric meshes of both solvers, even on non-coincident meshes.

First *CHARME* and *ASTRE* are coupled on the volume fluid domain, *CHARME* providing the local pressure p, temperature T and species number densities  $n_s$  to obtain the radiative power  $P_{rad}$ .

CHARME is also coupled with each of the MoDeTheC instances on the surface in contact with the fluid. For the liner, only the convective heat flux  $\varphi_{conv}$  is sent from CHARME to the MoDeTheC instance for the liner; the surface temperature  $T_w$ , the ablation energy flux  $\varphi_{ab,e}$  and the position of the points of the interface are exchanged in the other direction. For the electrodes, the boundary condition in CHARME takes into account the blowing of the degradation products; MoDeTheC instances for the electrodes then require the surface pressure and the mass fractions of species  $Y_s$  and will send also the mass flow rate  $\varphi_{gaz,m}$ , the gas temperature  $T_{gaz}$ , the interface porosity  $\varepsilon$ , the mass fractions of species  $Y_s$  and the ablation mass flux  $\varphi_{ab,m}$ .

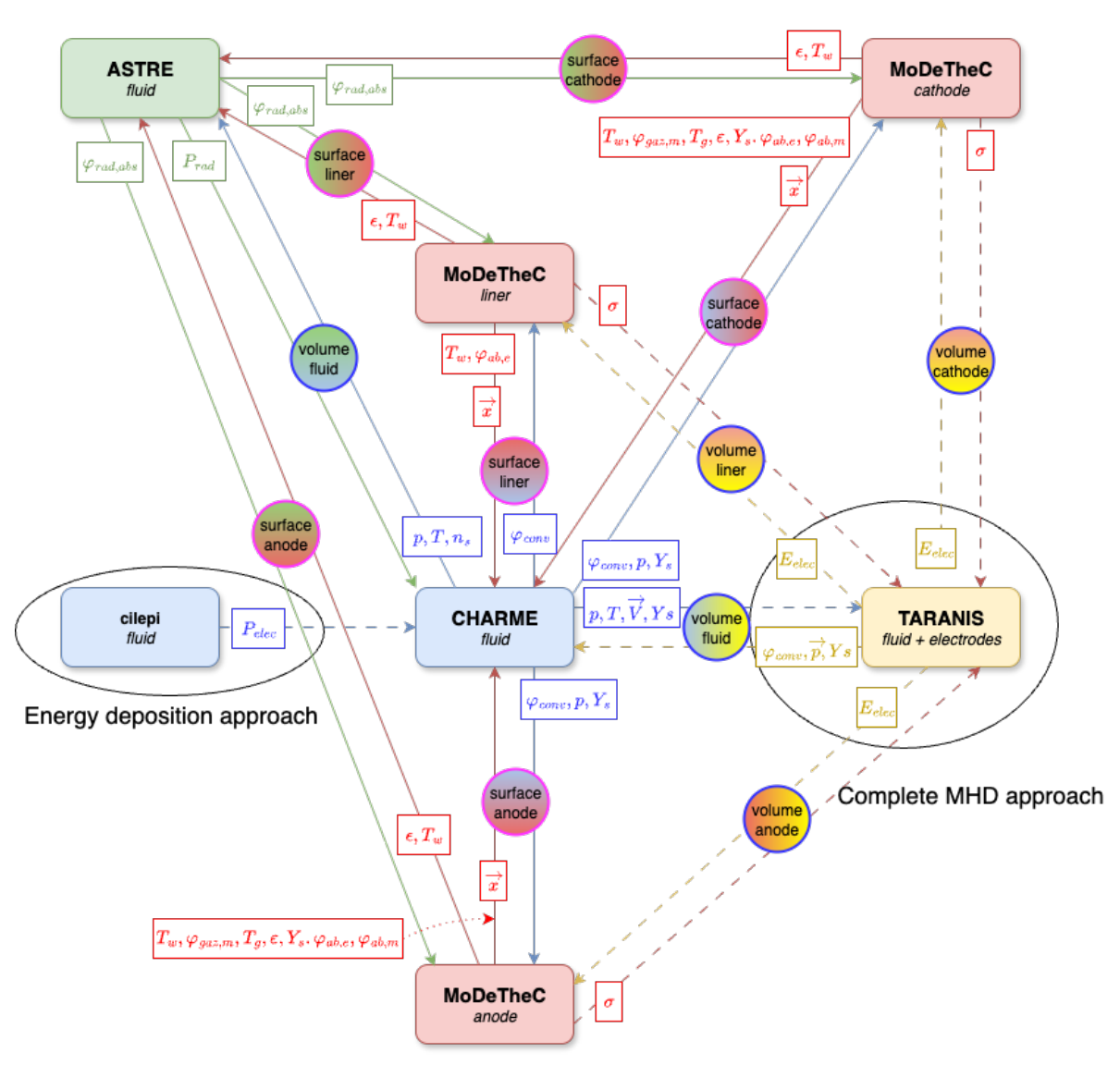


**Fig 8.** Scheme of the solvers used and their couplings using the *cwipi* library and the two retained approaches for energy injection

Finally, the three material parts are coupled with the radiative solver *ASTRE* on the surface in contact with the fluid, to provide the material emissivity  $\epsilon$  and wall temperature  $T_w$  required by the boundary conditions of the radiative solver and get in exchange the absorbed radiative flux  $\varphi_{rad,abs}$ .

## 2.2. Energy generation methods

The following simulations correspond to a shot that was performed in the experimental F4 facility in 2010. For this shot the current and the voltages between the ground and each electrode  $U_1$  and  $U_2$  have been measured, the resulting electrical power is the input of our calculation (figure 9b). Two methods have been set up to represent the rotating electric arc in the arc chamber.

## **Energy deposition approach**

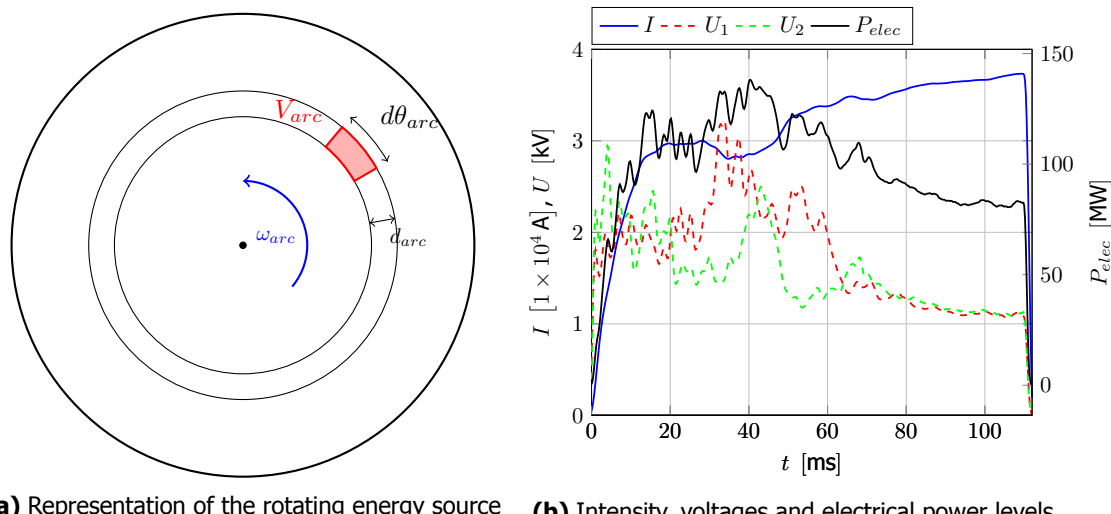
In a first approach the electric arc is represented by an unsteady volumetric source term as described in figure 9a. The power is homogeneously distributed in a part of a cylindrical shell positioned at a radius  $R_{arc}$  from the center of the chamber and spanning all the height of the chamber  $H_{chamber}$ . The shell has a radial extent  $d_{arc}$  and an angular section  $d\theta_{arc}$ . The volume power inside the source term  $P_{elec,V}$  is then given by :

$$P_{elec} = I (U_1 + U_2)$$

$$V_{arc} = 2\pi H_{chambre} R_{arc} d_{arc} \frac{d\theta_{arc}}{2\pi}$$

$$P_{elec,V} = \frac{P_{elec}}{V_{arc}}$$

Finally the source term is assumed with a rotation frequency  $f_{arc}$ . Few measurements are available for the rotation frequency of the arc. Thus, an estimate value of  $f_{arc}=1000\,\mathrm{rad}\,\mathrm{s}^{-1}$  was chosen, with  $\omega_{arc}=2\pi f_{arc}$  based on the order of magnitude established previously on figure 6.



- (a) Representation of the rotating energy source term representing the arc as seen from below
- **(b)** Intensity, voltages and electrical power levels injected inside the arc chamber

Fig 9. Scheme of the rotating energy source term and electrical power injected into the arc chamber

## **Complete MHD approach**

In the second approach, we aim to model the dynamics of the electric arc more accurately by directly solving the conservation of the electric current i in the domain (fluid and solids). This is achieved by solving for the electric potential  $\phi$  using the continuity equation  $\nabla \cdot \mathbf{i} = 0$ , coupled with the generalised Ohm's law  $\mathbf{i} = \sigma(-\nabla \phi + \mathbf{v} \times \mathbf{B})$ , where  $\sigma$  is the electrical conductivity,  $\mathbf{v}$  is the flow velocity and  $\mathbf{B}$  is the magnetic field. The conductivity depends primarily on the plasma composition, pressure and temperature. The magnetic field is computed using the Maxwell-Ampère equation, neglecting the displacement current:  $\nabla \times \mathbf{B} = \mu_0 \mathbf{i}$ . These equations are solved using ONERA's TARANIS code, whose further details are available in [10]. In this work, we present preliminary results from a simplified coupled approach, where TARANIS is interfaced with the CHARME solver. The MHD effects influence the plasma evolution through two source terms in the Navier-Stokes equations solved by CHARME: the ohmic heating term  $\mathbf{j}^2/\sigma$  in the internal energy conservation equation and the Lorentz force  $\mathbf{j} \times \mathbf{B}$  in the momentum conservation equation. These terms are computed by TARANIS and transferred to CHARME through cwipi at each time step, while CHARME provides pressure, temperature, mass fractions and velocity to TARANIS.

## 2.3. Case setup and numerical parameters

Considering the low velocities inside the chamber the flow is then considered laminar. The species composing the fluid are the 11 species of the Park model [11]:  $N_2$ ,  $O_2$ , N, O,  $N_2$ ,  $N_2$ ,  $O_2$ ,  $N_1$ ,  $O_2$ ,  $O_3$ ,  $O_4$ ,  $O_7$ NO<sup>+</sup> and e<sup>-</sup>. Each species follows a perfect gas law and their thermodynamics properties are given by [12].

HiSST-2025-79 ONERA F4 wind tunnel: history and simulations of the arc chamber The mesh for the flow domain is generated using Gmsh [13] with a hybrid strategy: a structured layer of hexahedra composes the area on which the arc passes and the rest of the domain is filled with tetrahedra (blue part on figure 10). The structured layer has 8 layers along the radius and 120 along the perimeter. The complete mesh is composed of around  $420\,000$  cells.

The chemical non-equilibrium Navier-Stokes equations are then solved with *CHARME*, with a time step  $dt_{\text{CFD}}=1\times10^{-6}\,\text{s.}$ 

## Radiation of the species

In the volume of the chamber the radiation of the species is also accounted for thanks to the solver *ASTRE*. It uses a Monte-Carlo method to simulate a semi-transparent medium, with a spectral method [14] for the radiative properties of the gas. The considered gas is a  $N_2$ - $O_2$  plasma, modelled with a statistical narrow-band model [15]. The temperature is initially imposed at  $293\,\mathrm{K}$  at every boundary of the domain for this solver assuming diffuse reflection and an emissivity of 1. With regards to the high calculation time per iteration of this solver, the radiation of the species had to be under-cycled compared to the CFD solver *CHARME*. A good compromise between calculation time and accuracy of the results was found with a time step of  $dt_{\rm rad} = 2 \times 10^{-4}\,\mathrm{s}$ .

## Heating and degradation of the liner

The liner is modelled by a  $5\,\mathrm{mm}$  cylinder around the chamber in which the heat conduction and the surface recession due to ablation are accounted for. In order to reduce the complexity of the simulation, a single graphite species is considered in this domain with constant properties. The ablation follows a law of fusion/sublimation at constant temperature of  $3900\,\mathrm{K}$ , with an ablation mass enthalpy of  $345\,000\,\mathrm{Jkg}^{-1}$ . The mesh of this domain is structured in the height and the width of the domain and contains  $15\,000\,\mathrm{nodes}$ . A time step of  $dt_{\mathrm{mat}} = 1 \times 10^{-5}\,\mathrm{s}$  is sufficient given the characteristic times of conduction and ablation.

#### **MHD**

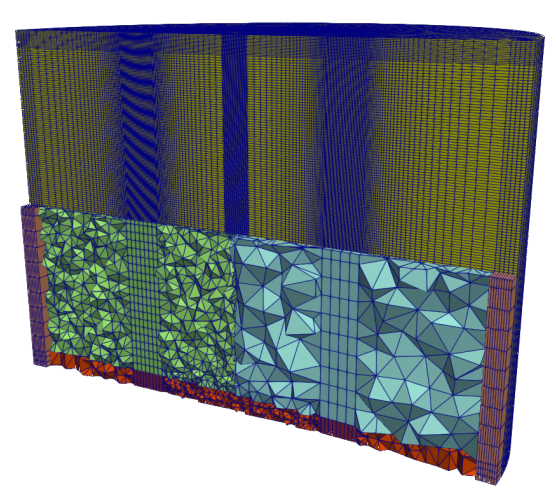
Within the MHD approach, as an initial step to demonstrate the working principle, we adopted a strategy commonly employed in atmospheric arc modelling for studying lightning effects [16]. The plasma is assumed to be in local thermodynamic equilibrium (LTE) and a single numerical species, referred to as "air," is used in our simulations. This air model incorporates the same species as in the energy deposition approach, with their fractions computed for given pressure and temperature conditions through Gibbs free energy minimization. Thermodynamic properties are derived from partition functions and transport coefficients are estimated using the Chapman-Enskog theory.

To accurately capture the structure of the electric arc, the mesh in this approach is significantly finer than that used in the energy deposition approach. The resulting mesh is displayed in figure 10b. To ensure robust current conservation, a structured, fully hexahedral mesh is employed. In the central annular volume between the electrodes (highlighted in red), the spatial resolution reaches  $375\,\mu m$ . The annular electrodes have a width of  $2\,cm$ , while the chamber has a radius of  $13.3\,cm$ . The distance between the electrodes is  $18\,cm$ . The electrical conductivity in the electrodes is set to that of copper,  $5.96\times10^7\,\mathrm{S\,m^{-1}}$ , while in the "liner," it is set to  $1\times10^{-4}\,\mathrm{S\,m^{-1}}$ . The initial background air conditions are set to a pressure of 30 bar and a temperature of  $300\,\mathrm{K}$ . All plasma-wall interfaces are treated as adiabatic boundaries for the fluid solver. The electric potential is arbitrarily set to 0 V at the bottom electrode and 1 V at the upper electrode. At each time step, the voltage difference (and consequently the current density) is rescaled to satisfy the imposed current value. In this approach we do not include radiative heat.

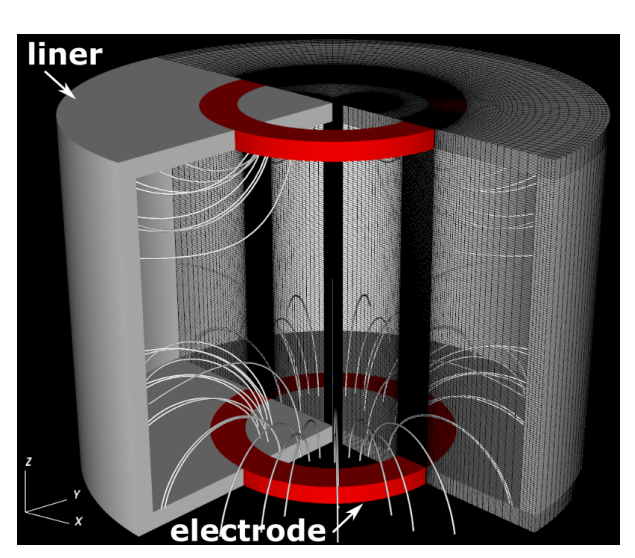
The primary objective of this demonstrative simulation is to showcase the self-consistent capture of arc rotation induced by Lorentz forces. To this end, we significantly simplified the electrode geometry. However, we accounted for a critical feature of the complex electrode geometry described previously: the spiral electrodes generate a magnetic field responsible for the azimuthal acceleration of the arc column via Lorentz forces. Here, we adopt a simplified approach by implementing two pairs of 4-turn coils positioned immediately behind the simplified electrodes. The resulting magnetic field, shown in figure 10b, is initialised by coupling *TARANIS* with the open-source Magpylib library [17]. For testing purposes, the current in the coils can, if necessary, be controlled independently of the imposed current into the electric arc. This setup corresponds to the anti-Helmholtz coil configuration commonly used as magnetic traps in atomic physics experiments [18].

## **Meshes and timesteps**

Each code participating on the coupling runs on its own domain, mesh and timestep, suited for each physical phenomenon modelled. The figure 10a presents a view of the meshes used for the present results and the table 1 gives the meshes details and time steps for each solver. The variables are exchanged by external coupling on the relevant surface or volume between two codes.



(a) Cut of the meshes in the energy injection approach with colors corresponding to the table 1



**(b)** Mesh and domain for the simulation of a rotating arc using the MHD approach

Fig 10. Domains and meshes for the energy injection and the MHD approaches

Code	Nodes	Cells	Timestep [ms]
CHARME	100 000	420 000	1
ASTRE	14 000	56 000	200
MoDeTheC_electrodes	20 000	58 000	10
MoDeTheC_liner	15 000	13 000	10
TARANIS	4 340 000	4 340 000	1

**Table 1.** Numerical parameters for each solver

# 2.4. Results and discussion related to the energy injection approach Pressure comparison

Because of the extreme conditions inside the arc chamber, measurements are very complex to perform, so only a measure of pressure is available in order to compare to our simulation. This measure is taken in two places inside the chamber  $p_A$  and  $p_B$ ; the pressure being very homogeneous inside the chamber these measures are very close.

Moreover, despite the numerous physical phenomena accounted for it has been observed that injecting the whole electrical power inside the chamber led to too high levels of pressure. This is why it was chosen to adapt the input power by a factor  $\alpha$  in order to fit the pressure; indeed, it is known that some power is lost in different ways that are not yet modelled in the present work. In particular using the energy injection approach, the modelling using an energy source term is an approximate representation of the arc, which is most probably thinner. Using the present simplified approach a very good agreement is obtained for an adapted power  $P_{elec,cor} = \alpha P_{elec}$  with  $\alpha = 24$ % as displayed in figure 11.

#### Influence of the degradation of the liner

The heat conduction and degradation of the liner induced by the convective and radiative (due to the

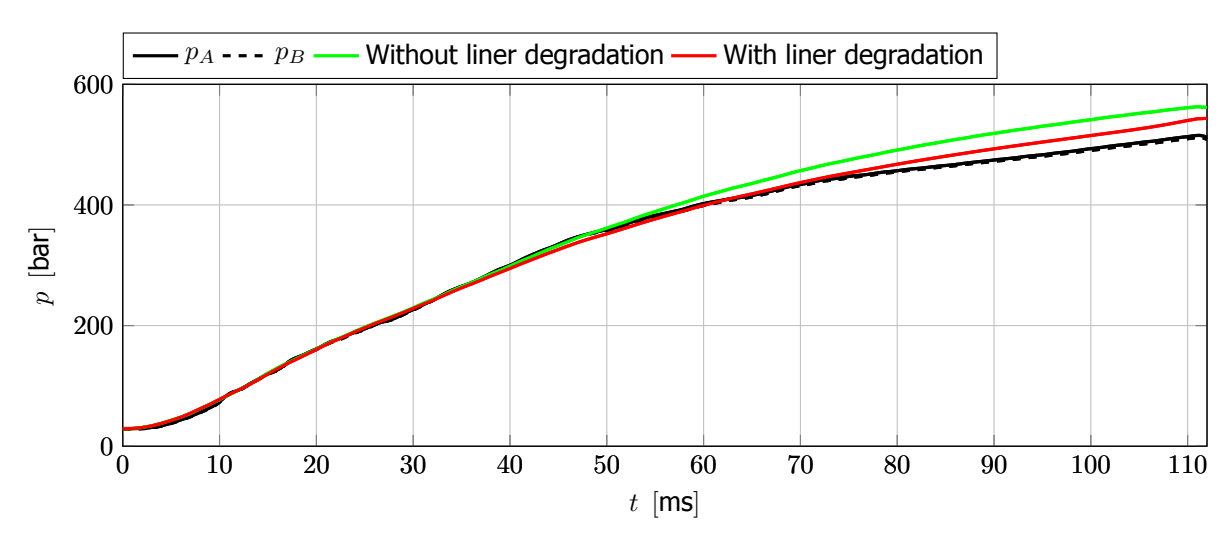


**Fig 11.** Comparison of the experimental (black, solid and dashed) and simulated pressure inside the chamber with (red) and without (green) degradation of the liner

species) heat fluxes are also accounted for, to represent the energy loss into the walls. The liner is made of a 2.5D carbone composite for which a model of sublimation at constant temperature at  $3900\,\mathrm{K}$  was assumed.

First, this seems to have a significative impact on the pressure of the chamber, fitting slightly better the measurements  $p_A$  and  $p_B$  as we can see on figure 11. In particular the pressure evolution bends from  $t=50\,\mathrm{ms}$ , time at which the conductive flux differs significantly from the case without degradation. The deviation from the measured pressure  $p_A$  at the end of the simulation is  $9.6\,\mathrm{\%}$  without the liner degradation and reduces to  $6.1\,\mathrm{\%}$  when accounting for it.

A comparison of the mean convective, conductive and ablation heat fluxes on the liner surface over the time is presented on figure 12. We can observe as expected that the convective heat flux is much lower than the conductive heat flux by at least 3 orders of magnitude. Initially the surface temperature is not sufficient to degrade the liner. Ablation occurs later from  $t=100\,\mathrm{ms}$ , with an ablation flux due to mass loss of around  $2\times10^7\,\mathrm{kWm}^{-2}$ .

The mass loss of the liner may be compared to the experimental; indeed the liner is a piece that was reused between several shots performed at the F4 facility. Over a period of 40 shots a mass loss of  $480\,\mathrm{g}$  have been measured, giving an average of  $12\,\mathrm{g}$  of mass lost per shot. Similarly, from the difference of volume of the liner before and after the calculation, a mass loss of  $15\,\mathrm{g}$  is calculated which compares well with the experimental estimate.

#### Temperature, species and rotation of the fluid

The simulation also provides the flow characteristics and the composition of the air inside the arc chamber. Figure 13 gives the evolution of the mean temperature over the perimeter of the arc, over the whole chamber volume, the maximum temperature reached in the fluid and the mean velocity magnitude of the fluid over the arc perimeter. Figure 14 presents the evolution of the mean mass fraction of the species in the chamber.

Firstly the simulation was performed for an arc thickness of  $d_{arc}=12\,\mathrm{mm}$  (cf. figure 9a) corresponding to solid lines on figure 13. It can be seen that the mean temperature over the chamber volume rises slowly up to  $6000\,\mathrm{K}$  and up to  $7000\,\mathrm{K}$  for the mean temperature over the arc perimeter. Locally the maximum temperature in the chamber can reach around  $11\,000\,\mathrm{K}$ . This is far less that expected for this type of electric arc, reflecting the lack of representativity of the energy injection approach: the energy being averaged in the volume of the source term, the local phenomena in the electric arc are not well represented.

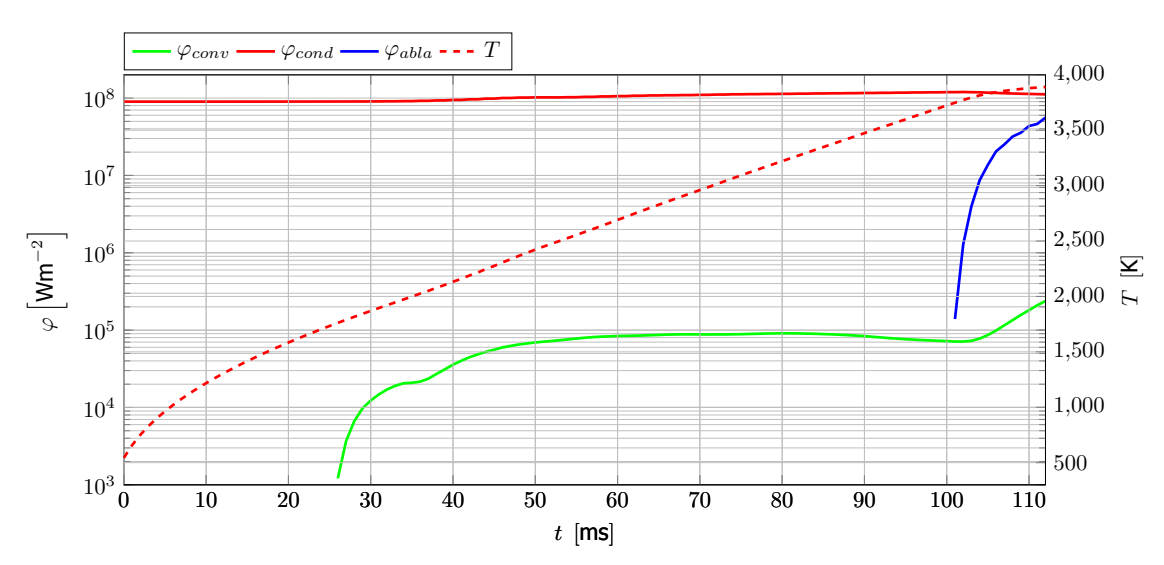


**Fig 12.** Evolution of the mean convective (green), conductive (red), ablation (blue) heat fluxes, and temperature (red, dashed) over the liner surface

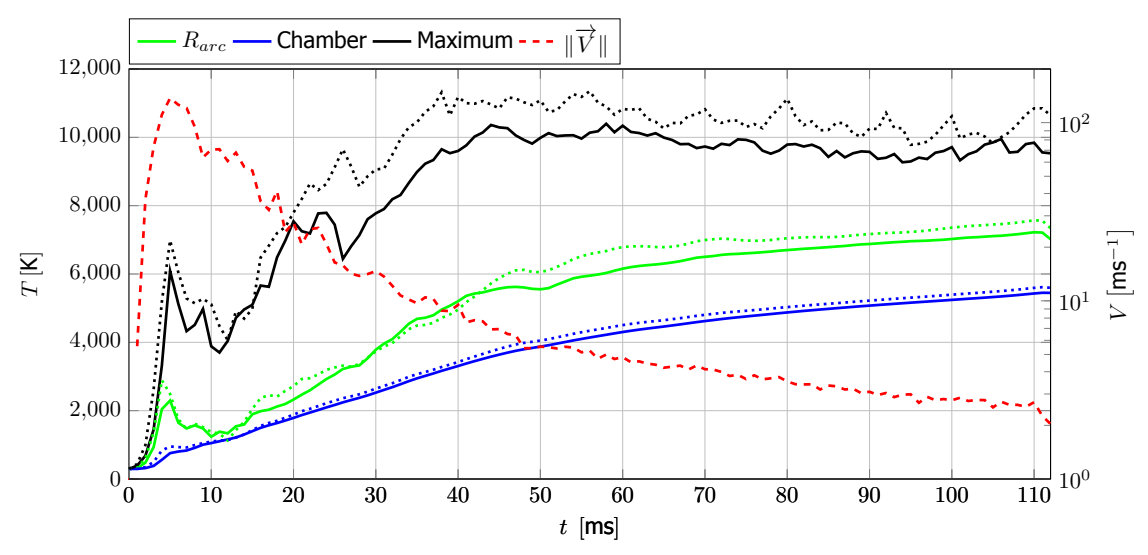


**Fig 13.** Maximum (black) and mean temperature over the perimeter of the arc (green) and over the whole volume (blue) and mean velocity magnitude over the arc perimeter (right, red, dashed) for  $d_{arc}=12\,\mathrm{mm}$  (solid) and  $d_{arc}=8\,\mathrm{mm}$  (dotted) for  $24\,\%$  of the input electrical power

This behaviour is confirmed by the trend obtained by reducing the volume of the energy deposition. The dotted lines on figure 13 give the evolution of the temperature for an arc radial extent of  $8 \, \text{mm}$  instead of  $12 \, \text{mm}$ , for which a slightly higher temperature level is obtained.

This weak description is highlighted by the evolution of the air composition on figure 14, for which only a few diazote dissociation is observed and almost no ionisation which would have also been expected and even mandatory for the arc to persist; however in this approach the arc is forced through the energy deposit so the lack of ionisation does not lead to extinction, but a severe underestimation of the radiative fluxes at the walls is most likely to occur. It is also to be reminded that the input electrical power was strongly limited in order to fit the pressure inside the chamber, which cause major difference in the temperature and air composition in the arc.

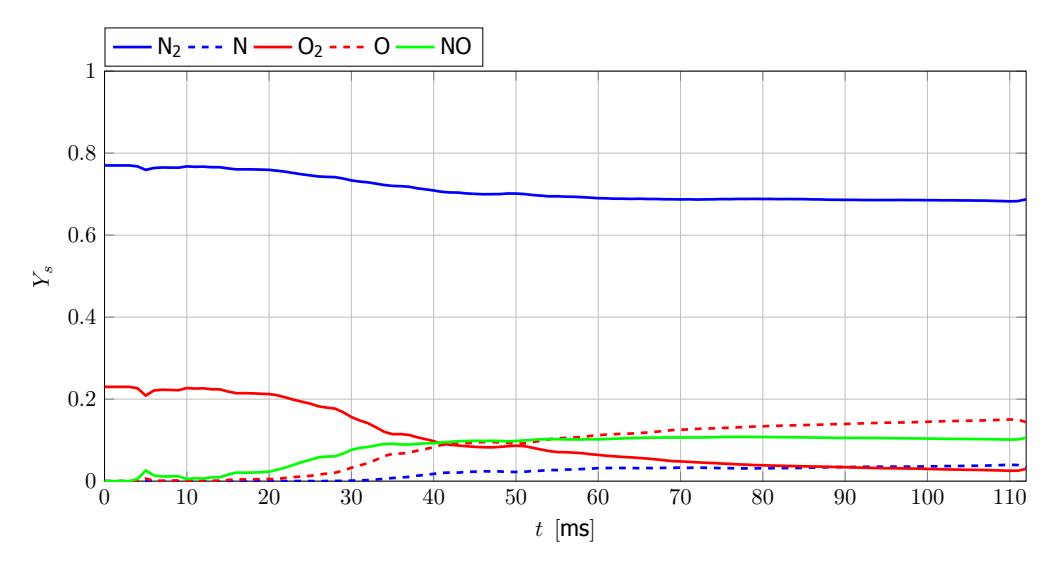


**Fig 14.** Evolution of the mean of the mass fraction of the main species in the chamber for 24 % of the input electrical power

#### 2.5. Preliminary results using the complete MHD approach

We present preliminary results obtained within the MHD approach. Since the initial gas breakdown is not modelled, an initial conductive path is required to allow current to flow before ohmic heating self-consistently establishes a hot, ionised and highly conductive column. This is achieved by imposing a high electrical conductivity in a small column spanning the electrodes for a brief period of 0.1 ms. The radial distribution of conductivity in the column follows a Gaussian profile with a peak value of  $500\,\mathrm{S}\,\mathrm{m}^{-1}$  at the column's center and a width of 2.5 mm. The time step is set to  $1\,\mu\mathrm{s}$  and the driving current is limited to  $1\,\mathrm{kA}$ . This limitation arises because, as noted earlier, radiative transfer is not included in this simulation—a critical feature for high currents, where radiative effects are expected to be non-negligible even at  $1\,\mathrm{kA}$ . To visualise the arc's evolution, figure 15 shows a 3D rendering of a temperature contour at  $T=8000\,\mathrm{K}$ .

The first image indicates that, within  $100\,\mu s$ , a hot plasma column with temperatures exceeding 8000 K forms in the initially forced region. By  $500\,\mu s$ , the arc feet near the electrodes begin rotating clockwise under the action of the Lorentz forces as depicted in figure 1b. A residual hot region, reminiscent of the initial forcing, remains visible. At later times, the arc column becomes increasingly distorted, with the feet significantly displaced around the electrodes. This effect results from stronger Lorentz forces near the electrodes, driven by a magnetic field that is 30–50 times stronger near the electrodes than at the column's center. The resulting azimuthal foot velocities are on the order of  $\sim 200\,\mathrm{m\,s^{-1}}$ . The arc's increasing elongation leads to an effective increase in its resistance by a factor of  $\sim 2.5\,\mathrm{between}\ 100\,\mathrm{and}\ 1800\,\mu s$  (from 0.8 to  $2.1\,\Omega$ ). This initial simulation demonstrates a promising approach to capturing the complex dynamics of the F4 rotating arc. Several tasks remain to enhance our current framework:

- computational time remains a limiting factor for modelling a full 100 ms F4 discharge. Potential solutions include optimizing the linear solver for current conservation calculations and implementing adaptive mesh refinement capabilities;
- radiative transfer must be incorporated to accurately model F4-relevant current levels ( $\sim 40$  kA);
- the arc's self-generated magnetic field should be computed, as it can significantly affect the column (e.g., feet jets, pinching, kinks);
- the CHARME-TARANIS framework should be coupled with the material degradation solver MoDeTheC.

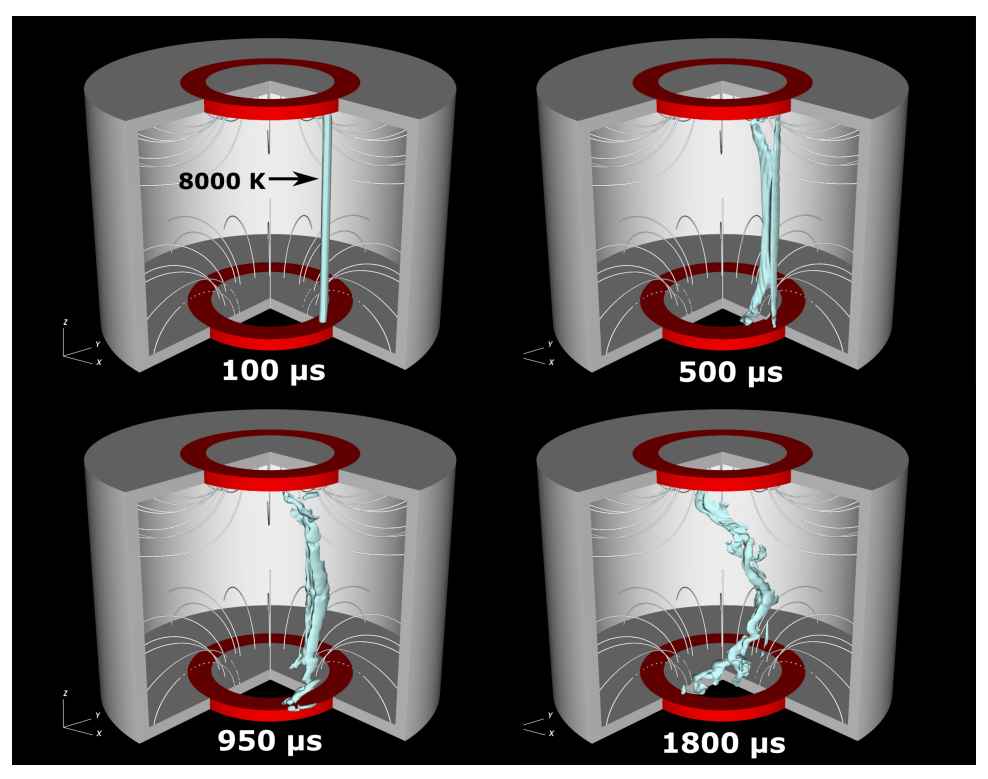


**Fig 15.** 3D rendering of the T = 8000 K isocontour at four different times: 100, 500, 950 and 1800  $\mu$ s

#### 3. Conclusions

After a brief history of the F4 high-enthalpy wind tunnel arc generation procedure, preliminary results of the modelling of the arc chamber have been presented. The first approach using energy deposition in the chamber has shown interesting results; the pressure inside the chamber could be fitted with a good agreement, however necessitating a significant correction on the input power. Several phenomena such as the radiation of the arc itself could be accounted for in order to improve the representativity of the simulation. The influence of the ablation of the liner have been studied and a good order of magnitude between the computed and experimental mass loss have been shown if we assume  $24\,\%$  of the total electric power. The principal limitation of this approach is the lack of modelling of the arc itself and its radiative heat transfer into the fluid and on the chamber wall material. In parallel, preliminary results using the complete MHD method have been presented, in which the arc has been put in rotation.

These exploratory works are to be completed in future simulations. First the degradation of the electrodes and the outgassing from them and from the liner will be added in order to quantify the pollution of the chamber before fluid expansion. Next, the MHD approach must be deepened to be able to simulate longer durations and add the radiative and material solvers to this coupling.

## References

- [1] A Refloch, B Courbet, A Murrone, C Laurent, J Troyes, G Chaineray, J B Dargaud, and F Vuillot. CEDRE Software. *Journal AerospaceLab*, (2):1–10, 2011.
- [2] Clément Le Touze. Couplage entre modèles diphasiques à « phases séparées » et à « phase dispersée » pour la simulation de l'atomisation primaire en combustion cryotechnique. PhD thesis, Nice, dec 2015.
- [3] Lionel Tessé, Francis Dupoirieux, Bernard Zamuner, and Jean Taine. Radiative transfer in real gases using reciprocal and forward Monte Carlo methods and a correlated-k approach. *International Journal of Heat and Mass Transfer*, 45(13):2797–2814, 2002.

- [4] Lionel Tessé, Francis Dupoirieux, and Jean Taine. Monte Carlo modeling of radiative transfer in a turbulent sooty flame. *International Journal of Heat and Mass Transfer*, 47(3):555–572, 2004.
- [5] L. Tessé and J.M. Lamet. Radiative Transfer Modeling Developed at Onera for Numerical Simulations of Reactive Flows. *Aerospace Lab*, (2):p. 1–19, mar 2011.
- [6] Nicolas Dellinger, Gillian Leplat, Cédric Huchette, Valentin Biasi, and Frédéric Feyel. Numerical modeling and experimental validation of heat and mass transfer within decomposing carbon fibers/epoxy resin composite laminates. *International Journal of Thermal Sciences*, 201(March):109040, 2024.
- [7] N. Dellinger, D. Donjat, E. Laroche, and P. Reulet. Experimental and numerical modelling of the interaction between a turbulent premixed propane/air flame and a composite flat plate. *Fire Safety Journal*, 141(June):103959, 2023.
- [8] Valentin Biasi. Modelisation Thermique de la Dégradation d'un Matériau Composite Soumis au Feu. page 201, 2014.
- [9] Éric Quémerais. cwipi, 2024. https://w3.onera.fr/cwipi/bibliotheque-couplage-cwipi [Accessed: 2025-08-27].
- [10] Aymeric Bourlet, Fabien Tholin, Julien Labaune, François Pechereau, Axel Vincent-Randonnier, and Christophe O. Laux. Numerical model of restrikes in gliding arc discharges. *Plasma Sources Science and Technology*, 33(1), 2024.
- [11] Chul Park, John T. Howe, Richard L. Jaffe, and Graham V. Candler. Review of chemical-kinetic problems of future NASA missions. II Mars entries. *Journal of Thermophysics and Heat Transfer*, 8(1):9–23, jan 1994.
- [12] M. Capitelli, G. Colonna, D. Giordano, L. Marraffa, A. Casavola, P. Minelli, D. Pagano, L. D. Pietanza, and F. Taccogna. Tables of internal partition functions and thermodynamic properties of high-temperature Mars-atmosphere species from 50K to 50000K. *European Space Agency (Scientific and Technical Reports) ESA STR*, (246):1–33, 2005.
- [13] Christophe Geuzaine and Jean-Francois Remacle. Gmsh, 2020. http://gmsh.info [Accessed 2025-08-29].
- [14] Jean-Michel Lamet, Philippe Rivière, Lionel Tessé, Anouar Soufiani, and Marie-Yvonne Perrin. Radiation modelling for air plasma in nonequilibrium conditions: application to earth atmospheric re—entry. sep 2008.
- [15] Jean Michel Lamet, Philippe Rivière, Marie Yvonne Perrin, and Anouar Soufiani. Narrow-band model for nonequilibrium air plasma radiation. *Journal of Quantitative Spectroscopy and Radiative Transfer*, 111(1):87–104, 2010.
- [16] F. Tholin, L. Chemartin, and P. Lalande. Numerical Investigation of the Interaction of a Lightning and an Aeronautic Skin During the Pulsed Arc Phase. In *International Conference on Lightning [amp] Static Electricity (ICOLSE 2015)*, pages 39 (6 .)—39 (6 .). Institution of Engineering and Technology, 2015.
- [17] Michael Ortner and Lucas Gabriel Coliado Bandeira. Magpylib: A free Python package for magnetic field computation. *SoftwareX*, 11:100466, 2020.
- [18] J. G.E. Harris, R. A. Michniak, S. V. Nguyen, W. C. Campbell, D. Egorov, S. E. Maxwell, L. D. Van Buuren, and J. M. Doyle. Deep superconducting magnetic traps for neutral atoms and molecules. *Review of Scientific Instruments*, 75(1):17–23, 2004.